Inversion of airborne geophysics over the DO-27/DO-18 kimberlites — Part 3: Induced polarization

Seogi Kang[1], Dominique Fournier[1], and Douglas W. Oldenburg[1]

Abstract

The geologically distinct DO-27 and DO-18 kimberlites, often called the Tli Kwi Cho (TKC) kimberlites, have been used as a testbed for airborne geophysical methods applied to kimberlite exploration. This paper focuses on extracting chargeability information from time-domain electromagnetic (TEM) data. Three different TEM surveys, having similar coincident-loop geometry, have been carried out over TKC. Each records negative transients over the main kimberlite units and this is a signature of induced polarization (IP) effects. By applying a TEM-IP inversion workflow to a versatile time domain EM (VTEM) data set we decouple the EM and IP responses in the observations and then recover 3D pseudo-chargeability models at multiple times. A subsequent analysis is used to recover Cole-Cole parameters. Our models demonstrate that both DO-18 and DO-27 pipes are chargeable, but they have different Cole-Cole time constants: 110 and 1160 μs, respectively. At DO-27, we also distinguish between two adjacent kimberlite units based on their respective Cole-Cole time constants. Our chargeability models are combined with the density, magnetic susceptibility and conductivity models to build a 3D petrophysical model of TKC using only information obtained from airborne geophysics. Comparison of this final petrophysical model to a 3D geological model derived from the extensive drilling program demonstrates that we can characterize the three main kimberlite units at TKC: HK, VK, and PK in three dimensions by using airborne geophysics.

Introduction

The Tli Kwi Cho (TKC) kimberlites were identified from a DIGHEM survey in 1992 (Figure 1). The kimberlites are located 28 km southeast of the Diavik Mine in the Lac de Gras region, Northwest Territories, Canada. The initial discovery targeted two anomalies, called DO-18 and DO-27. Following the initial discovery, several generations of electromagnetic (EM) systems have been deployed over the TKC area in an effort to characterize the kimberlites. In 1999, the first time-domain electromagnetic (TEM) survey was carried out using the AeroTEM I system (Boyko et al., 2001). Negative transients were measured, in particular at DO-18, although it was not clear whether these were true signals from the earth or instrumental noise. Surveys with new generations of equipment, AeroTEM II (2003) and VTEM (2004), reaffirmed the negatives. In addition, a ground loop NanoTEM (1993) survey showed negatives at the DO-18 pipe (Jansen and Doyle, 2000). Airborne TEM systems and NanoTEM have similar geometry and can be considered to be coincident loop systems, and hence the negatives are indicative of chargeable material (Weidelt, 1982). From the perspective of kimberlite exploration, however, the existence of an induced polarization (IP) signal is not necessarily significant. Ice and near-surface clays are known to be chargeable. Their presence distorts EM signals and impedes interpretation (Smith and Klein, 1996; Kozhevnikov and Antonov, 2012). As such, the existence of negative transients is usually considered to be "noise," and it is commonly referred to as IP contamination. However, recent studies have suggested that the negative transients could be attributed to more interesting geologic features, and thus the negative transients are "signal" (El-Kaliouby and Eldiwany, 2004; Flores and Peralta-Ortega, 2009; Kratzer and Macnae, 2012; Kang et al., 2014). It is this potential that we wish to pursue in this paper.

Kimberlite pipes in the Lac de Gras region are generally excellent geophysical targets because they exhibit high physical property contrasts with the granitic host rocks: higher magnetic susceptibility, lower density, and higher conductivity (Power and Hildes, 2007). The standard model adopted here for kimberlites consists of three different kimberlitic rocks: hypabyssal kimberlite (HK), volcaniclastic kimberlite (VK), and pyroclastic kimberlite (PK) as shown in Figure 2 and summarized in Table 1.

This paper is the third of a three-part series on TKC. In part 1 (Devriese et al., 2017), we presented the background

[1]University of British Columbia, UBC-Geophysical Inversion Facility, Department of Earth, Ocean, and Atmospheric Sciences, Vancouver, British Columbia, Canada. E-mail: skang@eos.ubc.ca; dfournie@eos.ubc.ca; doug@eos.ubc.ca.

Manuscript received by the Editor 8 September 2016; revised manuscript received 19 February 2017; published online 19 May 2017. This paper appears in *Interpretation*, Vol. 5, No. 3 (August 2017); p. T345–T358, 18 FIGS., 4 TABLES.

http://dx.doi.org/10.1190/INT-2016-0141.1.

history concerning the discovery and exploration of the region, the sequence of geologic models believed to be representative of the deposit, and the inversion and interpretation of the potential field data. The recovered 3D density and magnetic susceptibility models were shown to be valuable in defining the overall structural extent of the pipes and provided a case for defining three different rock units (granitic host, HK, and other more porous, lower density types of kimberlite). The gravity data were key in identifying kimberlite units in a background host. Within the volume of kimberlite, an HK unit was identified from the susceptibility model. The remainder of the pipe could be either a VK or a PK unit. From a potential fields standpoint, and without using geologic information, the distinction between PK and VK is ambiguous.

In part 2 (Fournier et al., 2017), we focused on a third physical property, electrical conductivity. The DIGHEM and VTEM data sets were inverted cooperatively by alternatively using either the DIGHEM result as a starting and reference model inverting VTEM data or vice versa. The final conductivity structure was somewhat dependent upon which data set was inverted last, but the two models were very similar. Two conductive pipes at DO-18 and DO-27 were imaged. For DO-27, we addressed whether the conductive anomaly was close to the surface, and perhaps caused by lake-bottom sediments and near-surface conductive rocks, or whether it was at depth. We concluded that the top of the conductive pipe was below the till layer. The conductivity model (after a DIGHEM inversion) was combined with density and magnetic susceptibility models to generate an updated petrophysical model having four rock units. This fourth unit, at the upper part of DO-27, likely corresponds to highly weathered VK or PK. It has a low density, moderate susceptibility, and moderate conductivity.

Here, in part 3, we concentrate upon extracting information from the IP signal in the VTEM data set. We apply our most recent TEM-IP inversion workflow (Kang and Oldenburg, 2016) and attempt to characterize the various kimberlite units based on their chargeability properties. Distinguishing between the three kimberlite units is crucial to get the most representative view of the TKC kimberlite pipes.

We first use the AEM data to illustrate the three fundamental steps of the workflow: (1) conductivity inversion, (2) EM decoupling, and (3) 3D IP inversion. The recovered 3D chargeability parameters are then interpreted in relation to the density, susceptibility, and conductivity models. In the final stage, we compare our petrophysical interpretation, based solely on airborne geophysical data, with the extensive drilling data available over the deposit. In particular, we also show how the recovered IP parameters of the rocks can help to distinguish between PK and VK units without any geologic constraints; this is valuable information in diamond exploration.

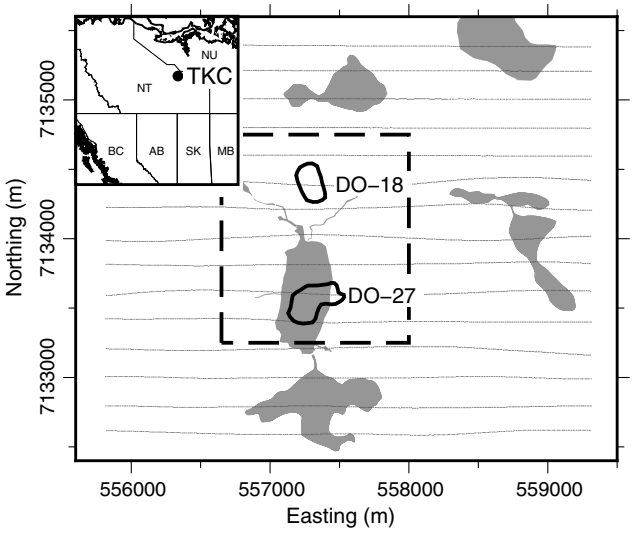

Figure 1. Location map for the TKC kimberlites, NWT. DO-18 and DO-27 are two main kimberlite pipes at TKC region.

Table 1. Expected physical property contrast for kimberlite deposits in the Lac de Gras region (Power and Hildes, 2007).

Rock type	Density	Susceptibility	Conductivity[2]
Glacial till	Moderate	None	Moderate-high
Host rock	Moderate	None	Low
HK	Low-moderate	High	Low-moderate
VK	Low	Low-moderate	Moderate-high
PK	Low	Low-moderate	Moderate-high

[2]Conductivity properties presented here do not take into account the ice content and temperature of rocks. As shown by Grimm and Stillman (2015), temperature and ice can significantly alter the bulk chargeability and the conductivity of rocks.

EM data

By simple visual inspection of the EM data, we note crucial features about the TKC kimberlites. From the

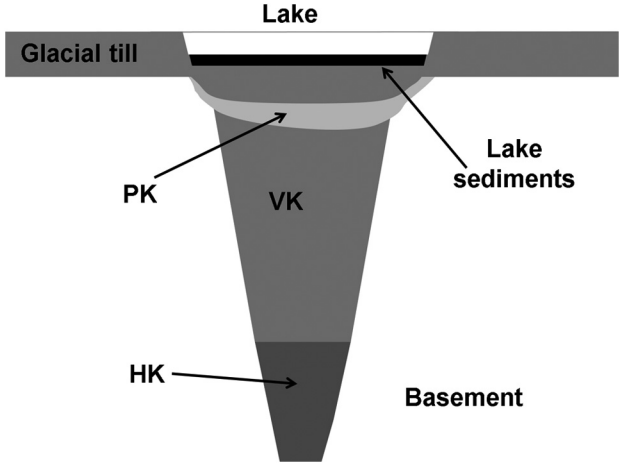

Figure 2. Schematic diagram of a kimberlite pipe in the Lac de Gras region (modified from Devriese et al., 2017). A lake may be present after glaciation and is often used as a first indicator of a possible kimberlite.

DIGHEM data at 7200 Hz, shown in Figure 4a, positive anomaly highs are observed over the location of DO-18 and DO-27, indicating that both pipes are more conductive than the host granitic rocks. Figure 3b–3d correspondingly shows NanoTEM (77 μs), AeroTEM II (26 μs), and VTEM (90 μs) data. All three TEM surveys show a positive anomaly near DO-27. We also identify three important anomalies that were not captured by the DIGHEM system and where the data are negative: A1 near DO-18, A2 between DO-18 and DO-27, and A3 near DO-27. Figure 4b–4d shows all three TEM data sets at later times. The NanoTEM (603 μs) and AeroTEM II data (534 μs) are significantly noisy. In the VTEM data (680 μs), however, the area that was previously positive at early times within DO-27 has switched to negative. We refer to this as the A4 anomaly, and it suggests that DO-27 has chargeable material.

Data quality and the time range for which data are sampled vary across EM systems, hence the EM data sets should show some differences. Figure 5a and 5b provides transients of NanoTEM and VTEM data at several sounding locations at DO-18, respectively. Soundings taken away from the pipe are referred to as "background." In NanoTEM data, all transients show negative values, but the negative transients from the background decay faster than those over the DO-18 pipe. The IP signal in the background soundings is likely due to surface glacial sediments (such as ice and clays). We are not able to identify these background negative transients in the VTEM data, likely because the VTEM system does not extend as early in time and also the survey equipment is higher off of the ground.

Because the VTEM data set includes most of the important IP features observed at TKC, while showing less noise at later time channels than other TEM data, we focus our analysis on the VTEM data. From these data, we identify four negative anomalies of interest (A1–A4), which also appear to be decaying at different rates as shown in Figure 5b. Before attempting to extract IP information from these data, we first need to separate the EM and the IP signals.

Decoupling the EM and the IP signal

The VTEM data presented in Figures 3d and 4d clearly show that a TEM measurement includes EM and IP signals. We want to extract the IP signal and invert it to recover chargeability. The observed datum d includes EM and IP effects and it can be expressed as

$$d = F[\sigma(t)], \tag{1}$$

where $F[\cdot]$ is the Maxwell operator. Here, $\sigma(t)$ indicates a time-dependent conductivity model. Often, this dispersive conductivity is defined in the Laplace domain, and it is written as

$$\sigma(s) = \sigma_\infty + \Delta\sigma(s), \tag{2}$$

where $s = \iota\omega$ is a Laplace transform parameter, σ_∞ is a conductivity at infinite frequency, and ω is the angular frequency (rad/s). Hence, the time-dependent conductivity can be obtained from the inverse Laplace transform of $\sigma(s)$: $\sigma(t) = \mathcal{L}^{-1}[\sigma(s)]$. Following Smith et al. (1988), the observed datum can be decomposed as

$$d = d^F + d^{\mathrm{IP}}, \tag{3}$$

where $d^F = F[\sigma_\infty]$ and d^{IP} are the fundamental and IP responses, respectively. The fundamental response, which does not have any IP effects, is the solution to Maxwell's equations using the conductivity at infinite frequency σ_∞, which is variable in 3D space. Assuming that we know σ_∞, we can obtain d^{IP} by subtracting d^F from d:

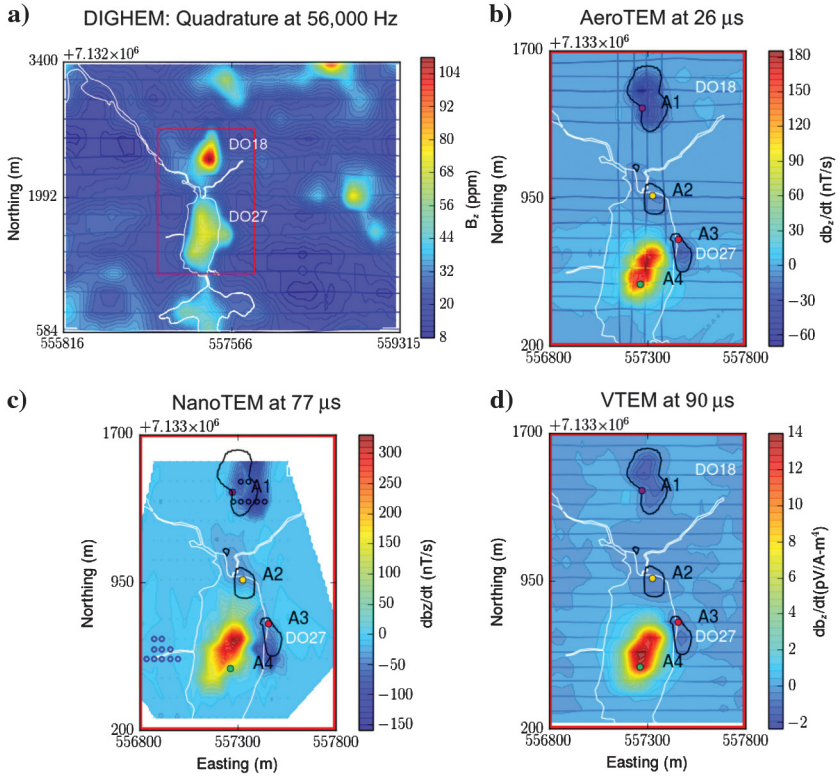

Figure 3. Plan maps of four EM data sets at TKC: (a) DIGHEM quadrature component (56,000 Hz), (b) NanoTEM (26 μs), (c) AeroTEM II (26 μs), and (d) VTEM (90 μs). For TEM data sets, a smaller region (red box) close to DO-18 and DO-27 is presented. The black line is a contour line of the negative anomaly (−8 nT/s) from AeroTEM data at 26 μs. The white line shows the boundary of the lakes. Negative anomalies: A1–A4 are correspondingly marked as purple, yellow, red, and green solid circles; A4 becomes negative in late time VTEM data as shown in Figure 4.

$$d^{\mathrm{IP}} = d - d^{F}. \tag{4}$$

This corresponds to EM decoupling.

Figure 6 shows an example of the observed, fundamental, and IP responses at a sounding location as a function of time computed by the EMTDIP code (Marchant et al., 2014). The sounding emulates a geologic model that is characteristic of a kimberlite pipe. The detailed information about this synthetic modeling example is described in Appendix A. At early times (<200 μs), d and d^F are almost coincident indicating an EM-dominant time ($|d^F| \gg |d^{\mathrm{IP}}|$). At late times, after 1000 μs, d and d^{IP} are almost coincident indicating IP-dominant times ($|d^{\mathrm{IP}}| \ll |d^F|$). Between 200 and 1000 μs, there are intermediate times when EM and IP effects are considerable ($|d^F| \simeq |d^{\mathrm{IP}}|$). This clearly shows a natural separation of EM and IP responses in time: EM induction is usually dominant at early times, but IP effects can be dominant at late times when EM effects have significantly decayed. This separation occurs because the buildup of polarization charges, which occurs when an electric field is applied, takes time (Smith and West, 1989; Macnae, 2015; Kang and Oldenburg, 2016). The separation of TEM signals into EM-dominant, IP-dominant, and intermediate zones will be a foundation of the following TEM-IP inversion workflow that we use to extract the conductivity and chargeability information from the VTEM data.

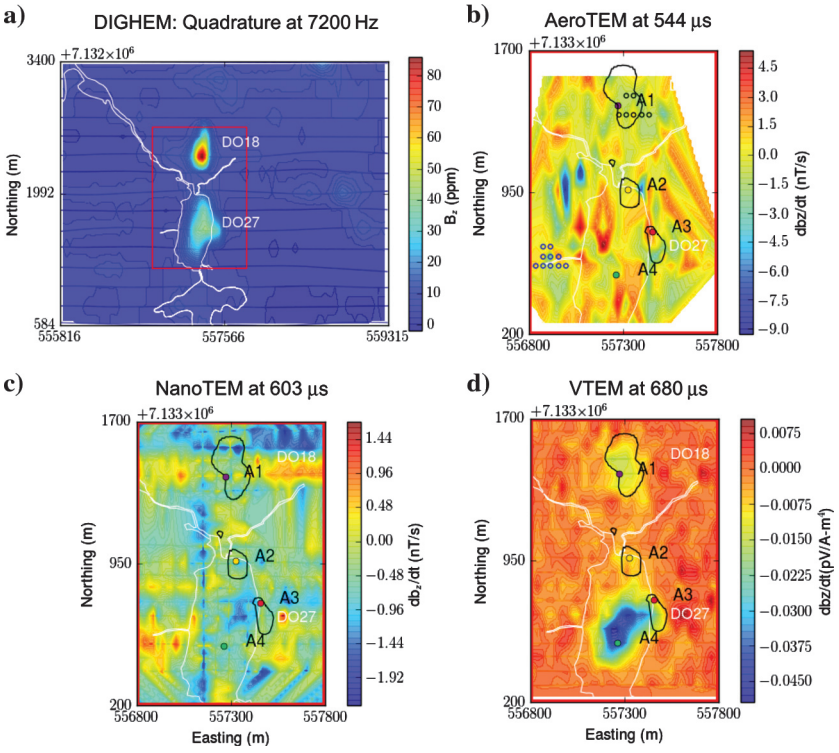

Figure 4. Plan maps of four EM data sets at TKC: (a) DIGHEM (56,000 Hz), (b) NanoTEM (603 μs), (c) AeroTEM II (544 μs), and (d) VTEM (680 μs). For TEM data sets, a smaller region (red box) close to DO-18 and DO-27 is presented. The black line is a contour line of the negative anomaly (−8 nT/s) from AeroTEM data at 26 μs. The white line shows the boundary of the lakes. Negative anomalies: A1–A4 are correspondingly marked as purple, yellow, red, and green solid circles; A1–A3 showed strong negatives for all TEM data in an early time.

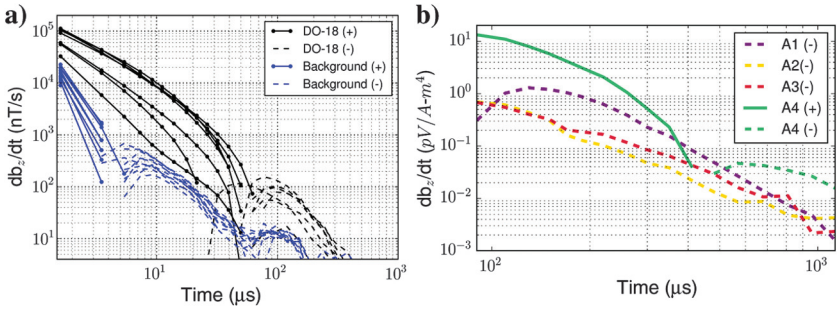

Figure 5. Transient curves of NanoTEM and VTEM data. (a) NanoTEM soundings away from the pipe and representative of background (blue lines) and over the DO-18 pipe(black lines). They are marked as blue and black solid circles in Figure 3b. (b) VTEM soundings at A1–A4 (correspondingly purple, yellow, red, and green lines). They are marked as purple, yellow, red, and green solid circles in Figures 3d and 4d. The solid and dashed lines distinguish positive and negative observations.

TEM-IP inversion workflow

To extract conductivity and IP information from the VTEM data, we follow the TEM-IP inversion workflow developed by Kang and Oldenburg (2016). This workflow includes four steps: (1) invert TEM data, and recover an estimated conductivity model σ_{est}. (2) Estimate the fundamental data $F[\sigma_{\mathrm{est}}]$ and subtract them from d; this generates raw IP data. (3) Using a linear form of the IP response, invert the raw IP data at multiple times to recover pseudochargeability. (4) Finally, consider a single cell at which pseudochargeabilities at multiple times have been obtained. Use a Cole-Cole model (Cole and Cole, 1941) to parameterize time-dependent conductivity, and solve a small inverse problem to estimate: η and τ with fixed c (either 1 or 0.5).

Conductivity inversion

The first step in the workflow is to estimate the background conductivity σ_∞ from the TEM data. Paper 2 (Fournier et al., 2017) of this series was devoted to this challenge. All of the DIGHEM data, and VTEM data that were positive, were cooperatively inverted. In some areas near DO-18, even the earliest time channels were negative so only DIGHEM data could be used there. The neglect of potential IP contamination in the DIGHEM

data, and the likelihood of IP contamination in VTEM time channels that were positve, probably contributed to the difficiulty we had in otaining a single conducivity that fit both data sets. However, the two models found through the cooperative inversion were very similar. For our puposes, where we concentrate on extracting information from the VTEM data, we use the inversion model obtained from the last step of the coopertive inversion in which the starting and reference model was from the DIGHEM data but the data to be fit were the VTEM data.

Figure 7 shows this estimated conductivity model σ_{est}. The two conductive pipes are imaged at depth. The conductive pipe for DO-27 extends deeper than the pipe for DO-18. Figure 8 shows plan maps of the observed d and the estimated fundamental responses $F[\sigma_{\text{est}}]$ at 130 μs. Regions in white correspond to negative data, and these soundings were not used in the coopertive inversion. Therefore, the conductivity structure near A1–A3 shown in Figure 7 is mostly coming from the DIGHEM data. The major region where the VTEM and DIGHEM data contributed to the final conductivity is near A4; d and $F[\sigma_{\text{est}}]$ in Figure 8 show a good match there.

EM decoupling

Based on the estimated conductivity σ_{est} from the previous conductivity inversion, we proceed with EM decoupling. Modifying equation 4 with σ_{est} yields

$$d^{\text{IP}}_{\text{raw}} = d - F[\sigma_{\text{est}}], \qquad (5)$$

where $d^{\text{IP}}_{\text{raw}}$ and $F[\sigma_{\text{est}}]$ are the raw IP data and the estimated fundamental data, respectively. From Figure 6, we expect that this decoupling step will only be effective at intermediate times, when EM and IP effects are considerable. Note that at early times (EM dominant; positive datum), d^{IP} is too small to be recovered, and at late times (IP-dominant; negative datum), EM decoupling will have a minor impact.

For the VTEM data, we compute $F[\sigma_{\text{est}}]$, and subtract this from d to yield $d^{\text{IP}}_{\text{raw}}$. Figure 9 shows time-decaying curves of d (black), $F[\sigma_{\text{est}}]$ (blue), and $d^{\text{IP}}_{\text{raw}}$ (red) at A1–A4. For A1–A3, as shown in Figure 9a–9c, even the earliest observation has a negative sign (IP-dominant time). The magnitude of $F[\sigma_{\text{est}}]$ is much smaller than $d^{\text{IP}}_{\text{raw}}$ except for the few earliest times, hence the impact of the EM decoupling is minor at these soundings. However, at A4 as shown in Figure 9d, we have a full suite of EM-dominant, intermediate, and IP-dominant times similar to the previous synthetic example as shown in Figure 6. The EM decoupling is most effective in the intermediate time (200–1000 μs).

We illustrate how our EM decoupling is effective by concentrating on two times: 130 and 410 μs. Plan view maps of d, $F[\sigma_{\text{est}}]$, and $d^{\text{IP}}_{\text{raw}}$ for the times are shown in Figure 10a and 10b. The two times are denoted by the vertical dashed lines in Figure 9. At 130 μs, near A4 we effectively removed the positive high anomaly (from the conductive DO-27 pipe) to reveal low-amplitude IP features. Near A1–A3, the EM-decoupling results in stronger negatives. At 410 μs, near A4, the EM decoupling makes a greater impact, and it converts positive

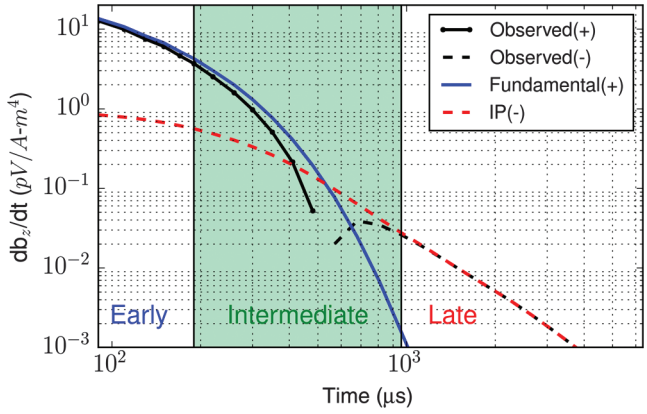

Figure 6. Time decaying curves of the observed (black line), fundamental (blue line), and IP (red line) responses. The solid and dashed contours distinguish positive and negative values.

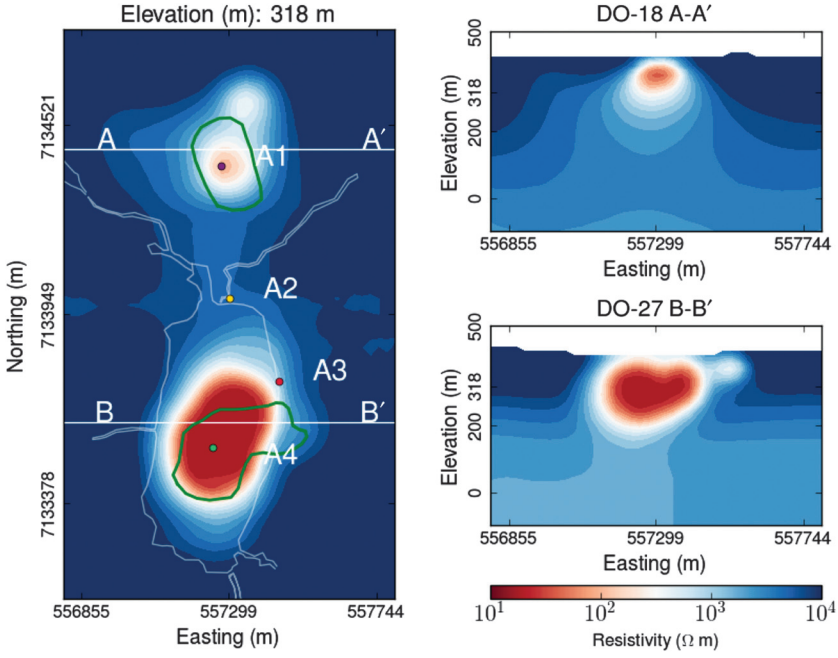

Figure 7. Plan and section views of the recovered conductivity model from the cooperative inversion of the VTEM and DIGHEM data sets. The left panel shows a plan map at 99 m below surface (318 m elevation). The top and bottom of right panels show A-A′ and B-B′ sections, respectively. The white outlines delineate boundaries of the lake. The green outlines show the extent of DO-27 and DO-18 at the surface, based on drilling. This figure is modified from Fournier et al. (2017).

observations to large amplitude negative IP data. Having separated the EM and IP signals in the VTEM data, the obtained $d^{\mathrm{IP}}_{\mathrm{raw}}$ at each time channel can now be inverted to recover at a 3D pseudochargeability. The inversion will be carried out for all time channels.

3D IP inversion

The IP data found in the above section can be related to pseudochargeabilty through the following linear equation:

$$\mathbf{d}^{\mathrm{IP}}(t) = \mathbf{J}\left(-\frac{\partial \tilde{\boldsymbol{\eta}}}{\partial \mathbf{t}}(t)\right), \tag{6}$$

where $\mathbf{J}$ is a sensitivity matrix depending on σ_∞, $\mathbf{d}^{\mathrm{IP}}(t)$ is a column vector for the IP data at an arbitrary time t, and $-\partial\tilde{\boldsymbol{\eta}}/\partial\mathbf{t}(t)$ is a column vector for the pseudochargeability s^{-1}. Here, the pseudochargeability is defined as

$$-\frac{\partial \tilde{\eta}}{\partial t}(t) = \frac{\partial}{\partial t}\left(\mathcal{L}^{-1}\left[\frac{\Delta\sigma(\mathrm{s})}{\sigma_\infty}\right] \otimes w^e(t)\right), \tag{7}$$

where $w^e(t)$ is a time history of electric field. Because $w^e(t)$ is a dimensionless property, the unit of the pseudochargeability will be s^{-1}. The computations of the sensitivity matrix and the time history of electric field for an airborne TEM problem are somewhat involved, but the detailed theoretical background for these computations is explained in Kang and Oldenburg (2016). The sensitivity matrix $\mathbf{J}$ is generated using σ_{est}. This only requires a single 3D TEM forward model and hence, once $\mathbf{J}$ is formed, $d^{\mathrm{IP}}_{\mathrm{raw}}$ can be inverted using linear inverse theory. The same sensitivity function is used for all time channels. To solve the linear inverse problem shown in equation 6, an open source geophysical simulation and parameter estimation package called SimPEG is used (Cockett et al., 2015).

We inverted all time channels of the $d^{\mathrm{IP}}_{\mathrm{raw}}$. The recovered pseudochargeabilities at two time channels: 130 and 410 μs are shown in Figure 11a and 11b, respectively. Four chargeable bodies are imaged close to the four IP anomalies, A1–A4, that were previously recognized. At 130 μs, three chargeable bodies close to A1, A2, and A3 are recovered, but none at A4 (DO-27).

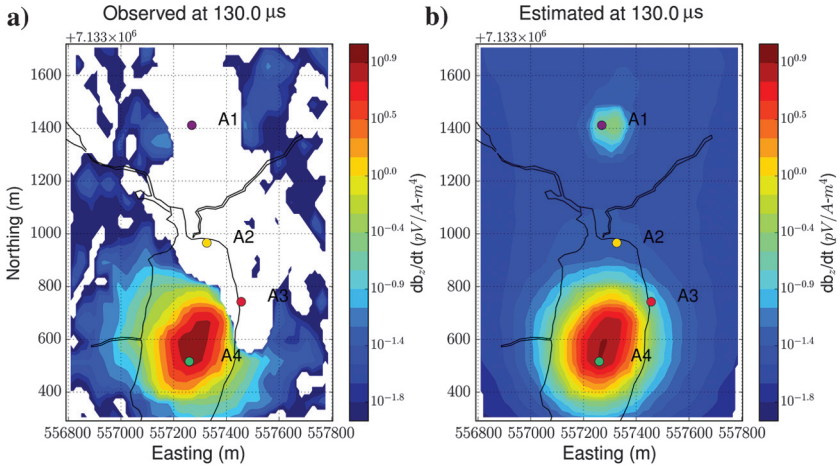

Figure 8. Observed and estimated fundamental responses at TKC. Four sounding locations at A1–A4 are marked as solid circles. Regions having negative values are shown as white.

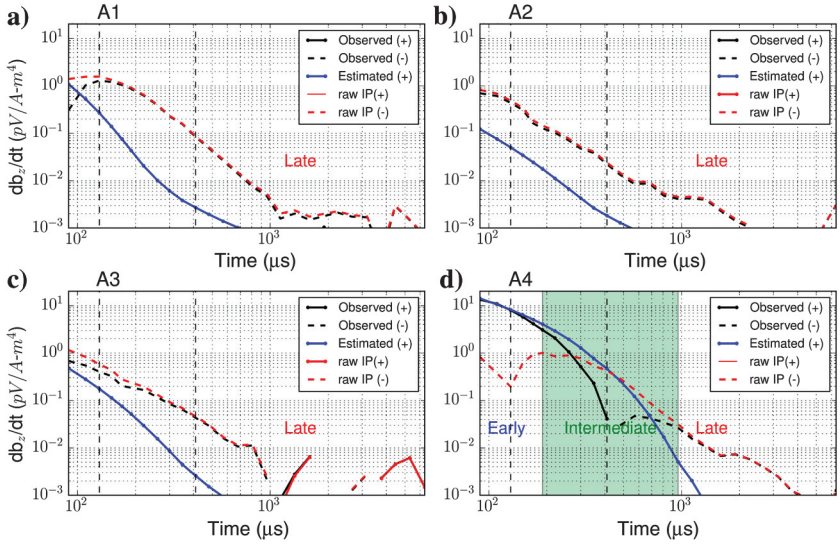

Figure 9. Time-decaying curves of the observed (black line), estimated fundamental (blue line), and raw IP (red line) data at (a) A1, (b) A2, (c) A3, and (d) A4. The solid and dashed lines distinguish positive and negative values. The vertical black dashed line indicates 130 and 410 μs, respectively.

At 410 μs, however, a chargeable body is imaged close to A4, whereas values of the other three chargeable bodies are significantly decayed. This reflects the different time decays associated with the IP signals: A1–A3 decay faster than A4.

To delineate boundaries of high pseudochargeability, we provide contours in which the pseudochargeability is 50 s^{-1} for the 130 μs (dashed red lines), and 10 s^{-1} for the 410 μs (solid red lines). The solid red contour clearly delineates the three chargeable bodies close to A1–A3, and the dashed red contour pertains to A4. Therefore, the three chargeable bodies close to A1–A3 (fast decay) can be distinguished from the one close to A4 (slow decay). In addition, at DO-27, two different chargeable bodies with vertical contacts can be delineated in the 3D volume (see B-B′ section in Figure 11b). Finally, at 130 μs, the chargeable body at A1 has the greatest strength, which can be differentiated from two bodies close to A2 and A3. Any distinction between A2 and A3 is subtle.

The recovered pseudochargeability at 130 and 410 μs provides some important information about the different kimberlites in the region. However, that IP information is still qualitative and hence it motivates the following quantitative analysis.

Extracting intrinsic IP parameters

We have recovered a distribution of pseudochargeability values at multiple times and we now wish to use those results to extract intrinsic information about the polarization parameters of the kimberlites. Pseudochargeabilities at representative cells close to A1–A4 anomalies are chosen and are shown as lines in Figure 12a. Using the procedure described in Kang and Oldenburg (2016), we fit $-\partial\tilde{\eta}/\partial t(t)$ using Pelton's Cole-Cole model (Pelton et al., 1978), which can be expressed as

$$\sigma(s) = \sigma_\infty - \frac{\sigma_\infty \eta}{1 + (1-\eta)(s\tau)^c}, \tag{8}$$

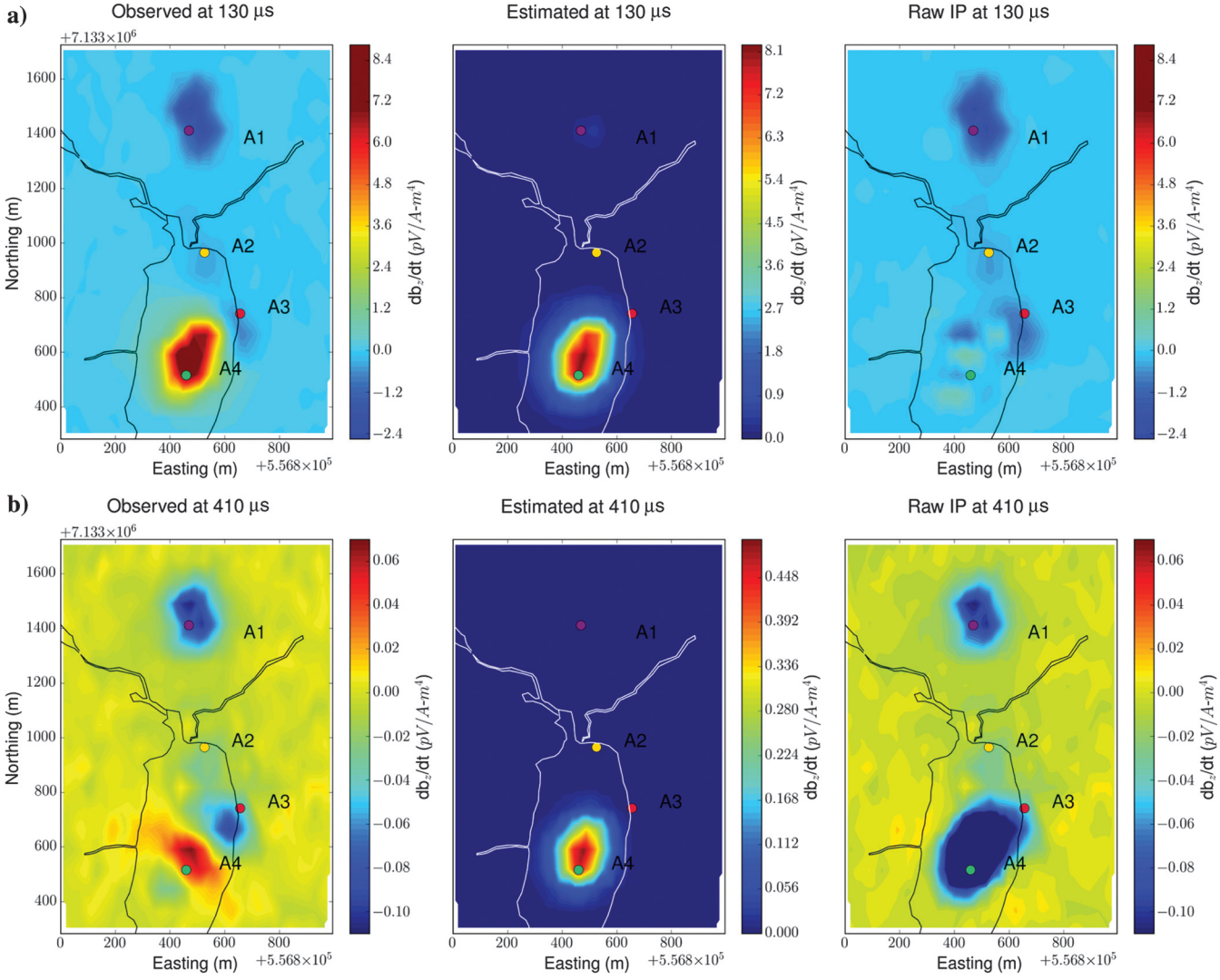

Figure 10. Plan maps of the observed, estimated fundamental, and raw IP data at (a) 130 and (b) 410 μs. Left, middle, and right panels correspondingly show the observed, estimated fundamental, and raw IP data.

where σ_∞ is the conductivity at infinite frequency (S/m), η is the chargeability, τ is the time constant (s), and c is the frequency dependency. A higher σ_∞ and η increases the amplitude of $\sigma(\omega)$ and results in a greater amplitude of the IP response. The decay rate of the IP response will be dependent mainly upon τ and c (e.g., the greater τ, the slower the decay rate).

In our analyses, two Cole-Cole parameters σ_∞ and c are assumed to be known, and so we are only estimating η and τ in this inversion. For σ_∞, the σ_{est} obtained from the conductivity inversion is used. We empirically use $c = 1$ for cells close to A1–A3 and $c = 0.5$ for those close to A4. The solid circles in Figure 12a show the predicted pseudochargeability; they match well with the observed pseudochargeability. Median values of the pseudochargeability at each time channel are shown in Figure 12b, and it demonstrates the different rates of decay between A1–A3 and A4. A summary of the estimated τ and η at each cell is presented in Table 2. Figure 13a shows a crossplot of the estimated τ and η for A1–A4. Clustering of A1–A4 indicates distinctions between the different kimberlite units based upon the estimated τ and η:

1) A4 can easily be distinguished from others by τ.
2) A1 and A3 can be differentiated by η and perhaps by τ.
3) The distinction between A1 and A2 is subtle, but it may be possible based upon τ values.

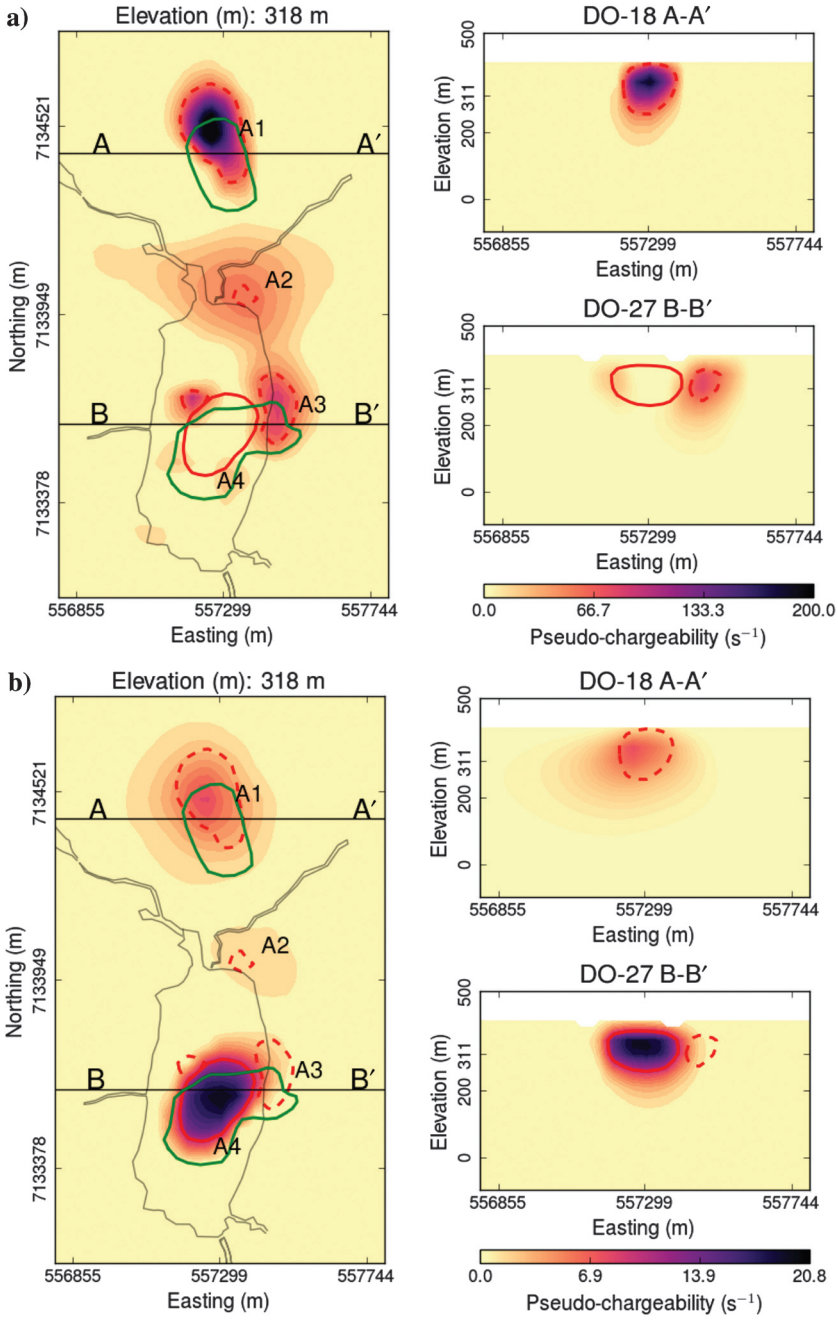

Figure 11. Plan and section views of the recovered pseudochargeability model from the 3D IP inversion of the raw IP at (a) 130 and (b) 410 μs, respectively. Left panel shows plan map at 99 m below surface (318 m elevation). Top and bottom of right panels show A-A′ and B-B′ sections, respectively. The solid and dashed red lines delineate contours of the recovered pseudo-chargeability at 50 s^{-1} (130 μs) and 10 s^{-1} (410 μs). The black outlines delineate boundaries of the lake. The green outlines show the extent of DO-27 and DO-18 at the surface, based on drilling.

Discussion

Consistent negative transients have been observed at TKC with various TEM surveys, including NanoTEM, AeroTEM II, and VTEM. These are due to chargeable materials. Focusing on the most recent VTEM data, we have identified four distinct IP anomalies showing different decaying features: A1–A3 decay faster than A4. We obtained raw IP VTEM data by implementing our EM-decoupling procedure and inverted the resulting raw IP data. The raw IP data were inverted to recover the 3D pseudochargeability at multiple time channels. Then, using representative cells from the four chargeable bodies, we fitted the pseudochargeabilities using a Cole-Cole model to recover η and τ.

Four chargeable bodies are imaged at depth, but in different time channels: chargeable bodies near A1–A3 are seen at 130 μs; chargeability near A4 is seen at 410 μs. The estimated τ for cells close to A4 is 1160 μs, and this is much greater than τ (approximately 70 μs) for A1–A3. The DO-18 pipe (A1) can thus be differentiated from the southern part of DO-27 (A4). The crossplots in Figure 13 also show that DO-18 is different (in τ and η)

from the northern part of DO-27. This again suggests that the two pipes are distinct events.

In addition, from the NanoTEM data, we have recognized that the background is also chargeable and that this is likely due to the ice. Figure 14 shows decay curves of the NanoTEM soundings away from the two pipes (thin lines), and a decay curve of a parametric fit using a half-space earth having Cole-Cole parameters (a thick line). The Cole-Cole parameters are $\sigma_\infty = 1.4 \times 10^{-4}$ S/m (approximately 7100Ωm), $\eta = 0.5$, $c = 1.0$, and τ is 18 μs. This τ is significantly smaller than the τ for the chargeable bodies close to A1–A3.

There are, at least, three different chargeable rocks that exist at TKC: overburden and two different kimberlite units. We believe that ice and clay are the main IP sources. The overburden at TKC is frozen, and hence ice can be an important IP source. An important question is whether the chargeability we attribute to kimberlite material is just a manifestation of ice. The NanoTEM data suggest that, away from the kimberlites, the background ice has a $\tau = 18$ μs. This value is smaller than any time constants shown in Figure 14, but the effects of temperature need to be considered. The polarization character of the ice significantly varies with temperature with τ decreasing as temperature increases (Grimm and Stillman, 2015). DO-27 is covered by a lake, and the VTEM data were acquired in the summertime. The temperature beneath the lake is likely higher than the wintertime temperature of the ground (when the NanoTEM data were acquired). We are left to conclude that we are imaging rocks in which the IP response is definitely different from ice. At DO-18, the source may be a frozen ice/clay mixture. At DO-27, where ice does not likely exist beneath the lake, the IP is likely caused by clays. The two units at DO-27 have distinctively different time constants. Considering that the pore size is proportional to τ, a greater pore size is expected for the southern part of DO-27 (A4) compared with kimberlites associated with A3.

Petrophysical model

From parts 1 and 2 of our series on TKC, we characterized the kimberlites based on 3D distributions of density, susceptibility, and conductivity. The low-density volumes were associated with kimberlitic material and in particular, with the two pipes at DO-18 and DO-27. The magnetic susceptibility showed that the two pipes were different. DO-18 was characterized as a pipe with moderate susceptibility, whereas DO-27 was dominated by a highly susceptible unit that was likely HK. High conductivity volumes, found in the upper parts of the two pipes, likely correspond to highly weathered PK or VK. However, based on these physical properties, it was not possible to distinguish between those units without geologic information from drillings (Devriese et al., 2017).

In this study, we have generated pseudochargeability models at 130 and 410 μs. We refer to the model for

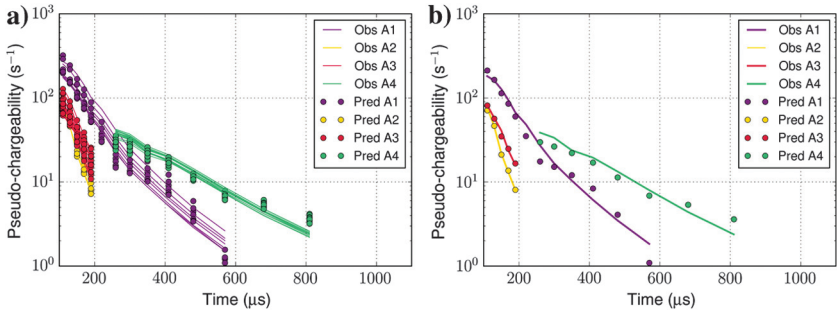

Figure 12. Comparison of the observed (lines) and predicted (solid circles) pseudochargeability at cells close to A1–A4 (correspondingly purple, yellow, red, and green colors). (a) All time-decaying curves of the observed and predicted pseudo-chargeability. (b) Median values of the observed and predicted pseudochargeability at each time.

Table 2. Median and standard deviation of estimated τ (μs) and η for A1–A4.

Division	Mean (τ)	Mean (η)	Standard deviation (τ)	Standard deviation (η)
A1	110	0.4	24	0.13
A2	50	0.4	9	0.11
A3	40	0.12	9	0.07
A4	1600	0.15	380	0.1

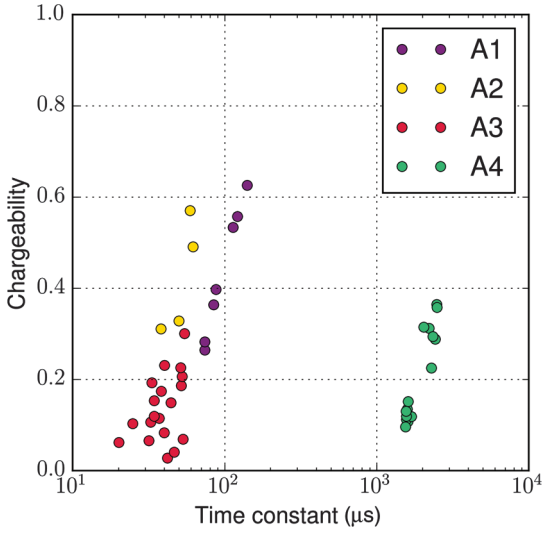

Figure 13. A crossplot between the estimated time constant τ and chargeability η at cells close to A1–A4. The solid circles shaded as purple, yellow, red, and green colors correspondingly indicate A1–A4.

130 μs as the early pseudochargeability $\tilde{\eta}_E$ and the model for 410 μs as late pseudochargeability $\tilde{\eta}_L$. These were distinctly different and show that DO-27 is composed of at least two different rock units.

Our goal is to combine these two chargeability models with the previous density, susceptibility, and conductivity models and build a final 3D petrophysical model over the TKC kimberlites that has been derived from only airborne geophysics.

Figure 15a shows overlaid anomalous values from all five physical property models. At DO-18, four different anomalies: density, susceptibility, conductivity, and $\tilde{\eta}_E$ are overlaid, which indicates that all of the airborne geophysics used at TKC can delineate the DO-18 pipe. At DO-27, high susceptibility (yellow) allows us to distinguish the HK unit. Two more rock units can be identified from $\tilde{\eta}_E$ and $\tilde{\eta}_L$. Using the union of all five physical property distributions, a petrophysical model with six rock units: R0–R5 is built and shown in Figure 15b; five units: R1–R5 are related to kimberlites having low density, whereas R0 indicates the granitic host rock. Table 3 summarizes our interpretation about the petrophysical model. R2 corresponds to HK. R3–R5 commonly have moderate susceptibility and conductivity, hence they could be either PK or VK based upon a general physical property information for Lac de Gras region shown in Table 1. However, with the chargeable information in $\tilde{\eta}_E$ and $\tilde{\eta}_L$, R5 can be distinguished from R4.

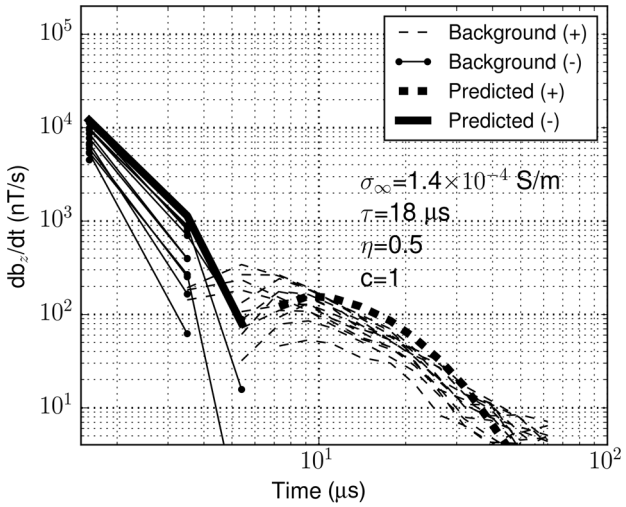

Figure 14. Transient curves of NanoTEM data, and predicted data from parametric fit of Cole-Cole model assuming half-space earth.

PK is a subclass of VK and is deposited after an explosive event. Both units can be highly weathered, resulting in significant clay content that is conductive and chargeable. Because of its explosive origin, PK likely has greater pore size than VK. The pore size of the rock is strongly correlated with the time constant: Greater pore sizes result in larger time constants (Pelton et al., 1978; Revil et al., 2014). From spectral analyses of the recovered pseudochargeability model, we have estimated the time constant of four anomalies: A4 has greater τ than A1–A3. With these results and the expected relative pore sizes for PK and VK material, our interpretation is that R5 (which has a large τ and is primarily located at A4) is a PK unit. R4 (which has a small τ and is located at A1 and A3) is a VK unit. At DO-27, R3, located below R4 and R5, indicates a highly weathered part of the kimberlite pipe, but determining whether this unit is PK or VK is not clear. Further, sensitivity of the EM and the IP data is limited in depth, hence labeling R3 as a different rock type is an overinterpretation. Similarly, the R1 unit, which is below R3, is interpreted as a kimberlite unit, but the type was not specified because its existence arises mostly from the density model, and that method lacks depth resolution. Overall, three distinctive kimberlite constituents within the TKC region — HK, VK, and PK — are distinguished and delineated in a 3D volume, and chargeable information obtained from the VTEM data has made a major contribution to distinguish between the PK and VK units.

Ground truth

Extensive drilling programs have been carried out at TKC, from which four different kimberlite units have been identified (Doyle et al., 1999; Eggleston and Brisebois, 2008):

1) dipping sheets of HK facies limited to the northeastern part of DO-27
2) shale-rich VK crater facies in the northern part of DO-27
3) resedimented PK crater facies infilling the core of DO-27
4) xenocryst-rich volcaniclastic kimberlite (XVK) crater facies mostly restricted to the core of DO-18.

Figure 16a and 16b compares plan maps of our final petrophysical model (100 m below the surface) to the geology based upon drilling results from an

Table 3. Petrophysical domains built from inversions of airborne geophysical data sets. Here ρ, κ, σ, $\tilde{\eta}_E$, and $\tilde{\eta}_L$ correspondingly indicate density, susceptibility, conductivity, pseudochargeability at 130 and 410 μs.

Rock unit	ρ	κ	σ	$\tilde{\eta}_E$	$\tilde{\eta}_L$	τ	Interpretation
R0	Moderate	Low	Low	Low	Low	N/A	Host rock
R1	Low	Low	Low	Low	Low	N/A	Kimberlite
R2	Low	High	Low	Low	Low	N/A	HK
R3	Low	Moderate	Moderate	Low	Low	N/A	PK or VK
R4	Low	Moderate	Moderate	High	Low	Small	VK
R5	Low	Moderate	Moderate	Low	High	Large	PK

extensive drilling program. The agreement is quite good particularly regarding the geometric confinement of the pipes. For the DO-27 pipe, interpretation of R2, R4, and R5 as, respectively, HK, VK, and PK agrees with the ground truth. From the comparative sections at DO-27 (B-B′) shown in Figure 17a–17c, the upper part of the PK and VK units is well-imaged with R4 and R5, respectively. The deeper part of the PK unit, which corresponds to R3 and R4, was not well distinguished in our interpretation due to the lack of depth sensitivity of the airborne geophysics (Smith, 1988; Macnae, 2015). The HK unit agrees well with R2 on the plan map (Figure 16), whereas in the B-B′ section shown in Figure 17. R2 is deviated from the HK unit. This discrepancy between R2 and HK in the section may be caused by the low resolving power of our smooth inversion for recovering the geometry of thin dipping sheets (HK). In addition, our interpretation that the DO-18 pipe is VK is reasonable. XVK is a subunit of VK and was identified through drilling. Overall, our analysis has clearly demonstrated the impact of using 3D IP information in an interpretation.

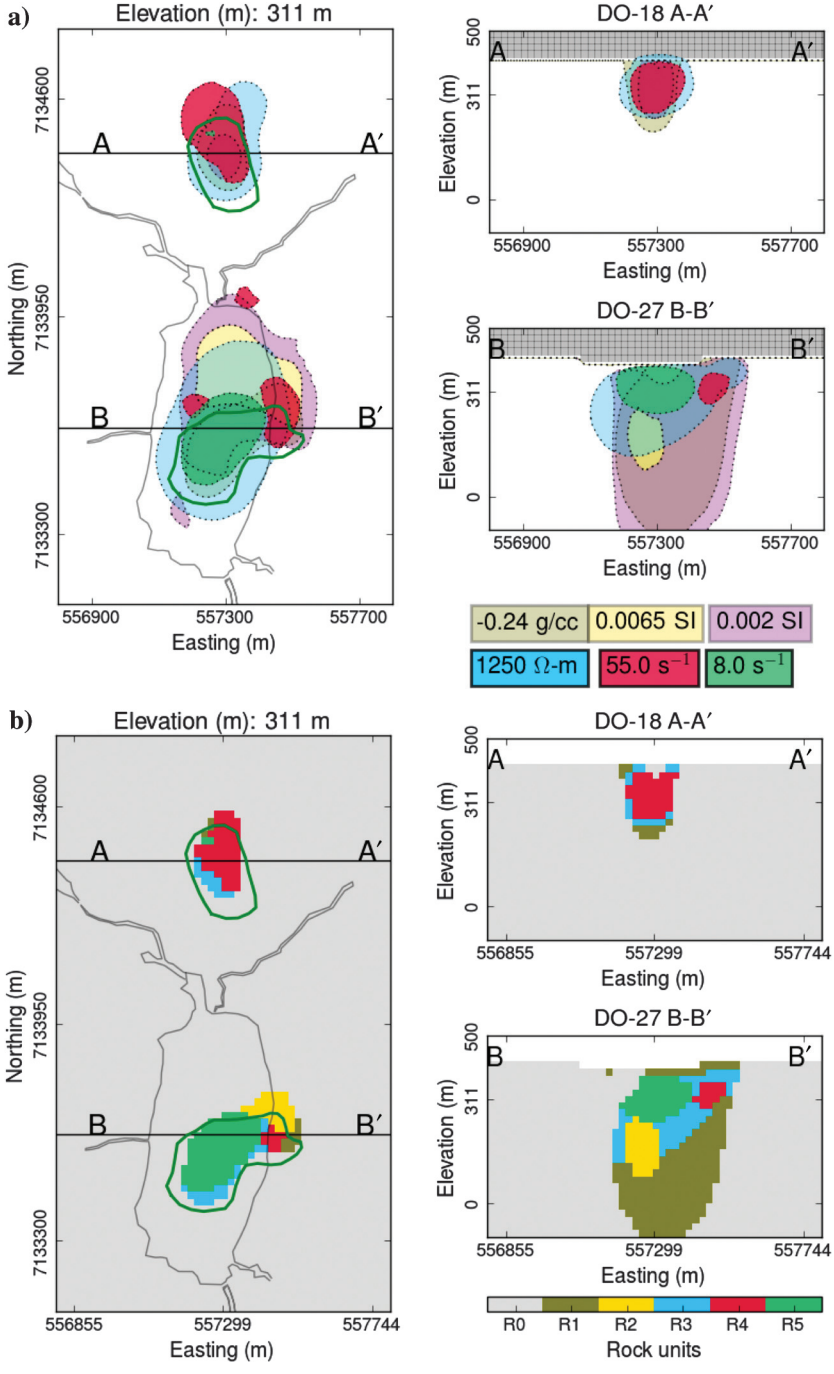

Figure 15. Comparative sections through the TKC kimberlites. (a) Overlaid anomalies of five physical property models: density constrast (olive), susceptibility (yellow and purple), conductivity (blue), pseudochargeability at 130 (red), and 410 μs (green). (b) Generated petrophysical model from five anomalies. The white outlines delineate boundaries of the lake. The green outlines show the extent of DO-27 and DO-18 at the surface, based on drilling.

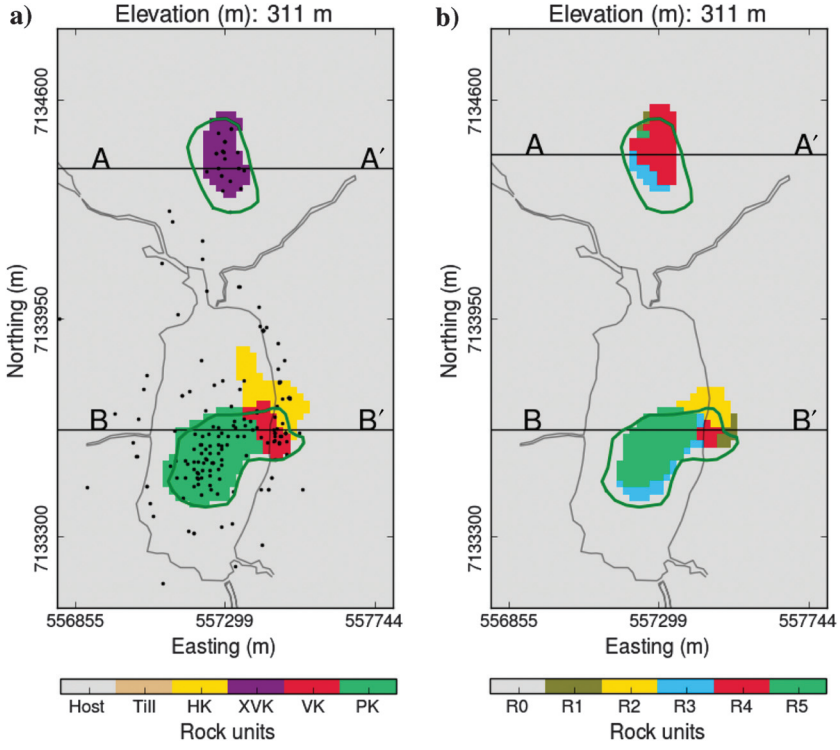

Figure 16. Comparative plan maps at 311 m elevation (approximately 100 m below the surface) through the TKC kimberlites. (a) The 3D geologic model obtained from the known geology and drilling results at the TKC area. (b) The 3D petrophysical model obtained from geophysics. The black outlines delineate boundaries of the lake. The green outlines show the extent of DO-27 and DO-18 at the surface, based on drilling.

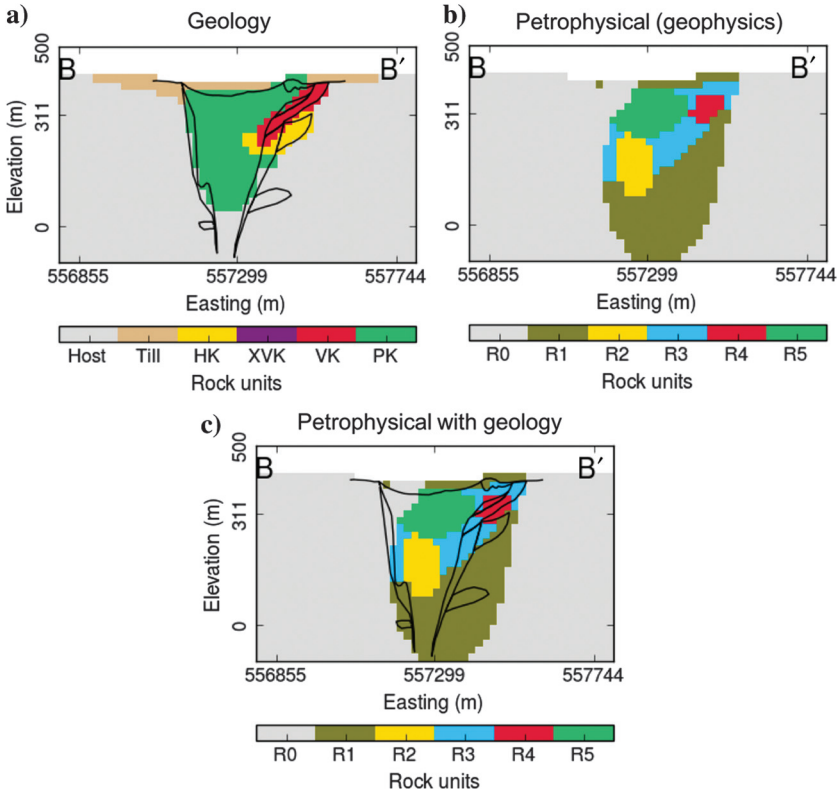

Figure 17. Comparative sections over DO-27 (B-B′). (a) The 3D geologic model obtained from the known geology and drilling results at the TKC area. (b) The 3D petrophysical model obtained from geophysics. (c) Petrophysical model with geologic boundaries. Geologic boundaries of rock units from Harder et al. (2008) are presented as black lines.

Conclusions

Airborne geophysical surveys such as magnetic, gravity, and EM have been carried out at TKC, and from parts 1 and 2, three physical property models such as density, susceptibility, and conductivity were generated. Building upon these models, we added the recovered pseudochargeability models at 130 and 410 μs to our interpretation, and generated a 3D petrophysical model at the TKC kimberlites. Five rock units related to kimberlites were used. Kimberlites are distinguished

by their low density, and the HK was delineated by the high susceptibility. The moderate conductivity at the upper part of the two pipes suggested that this was a highly weathered kimberlitic rock that might be PK or HK, but we were not able to differentiate between those units. The addition of IP information, however, enabled us to make this distinction because the two rocks have greatly different time constants. Our final petrophysical model was compared with the 3D geologic model built up from an extensive drilling program; the two models are quite similar. Only the XVK unit and the bottom part of the PK were not resolved.

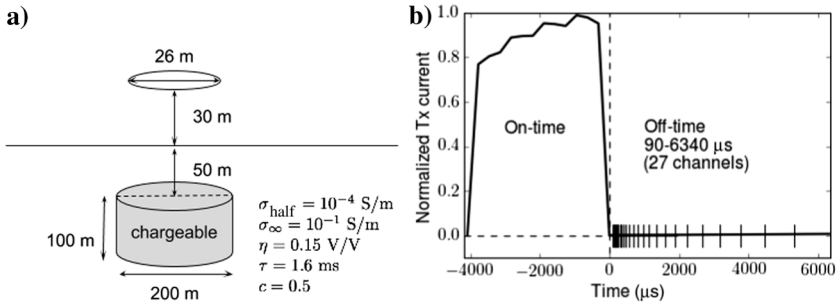

Figure A-1. (a) Geometry of a simple kimberlite pipe model with Cole-Cole parameters with the VTEM coincident-loop. (b) The current waveform for the TKC VTEM data.

In our three papers, no explicit information regarding the known geology has been used to constrain the inversion. Only the general kimberlite model, the component rock types, and their relative physical property contrasts were incorporated. Despite that, we obtained a rock model whose major features were representative of the geologic model obtained from drilling. All of the data used in the analysis were obtained from airborne surveys, which are far easier, and less costly, to collect than ground data. We note that if a single borehole had been drilled in the heart of the DO-27 pipe, then the geologic intepretation of the geophysical data would have greatly benefited; this could have had a major impact upon the exploration program. Moreover, an even greater benefit would have been achieved if that borehole had been logged petrophysically and also used to carry out a surface-to-borehole EM survey, perhaps using a large ground loop.

Acknowledgments

We would like to thank K. Witherly and J. Jansen for the stimulating discussions about the TKC data sets during the past 15 years and for identifying the challenges for inverting and interpreting these data. We also thank J. Pell, B. Clements, B. Doyle, T. Arvanis, and R. Enkin for discussions about the data and geologic interpretations. We especially thank Condor Geophysics, Peregrine Diamonds, and Kennecott for making the data sets available for our research. Finally, we are indebted to other UBC-GIF members for their efforts on this two-year project: S. Devriese, K. Davis, M. S. McMillan, D. Bild-Enkin, N. Corcoran, D. Cowan, L. Heagy, D. Marchant, L. A. C. Mata, M. Mitchell, and D. Yang.

Appendix A

Synthetic Example

We carry out a forward modeling with a simple pipe model shown in Figure A-1a with the VTEM setup. The VTEM system has a 26 m diameter transmitter loop and a coincident receiver loop. The system is flown 30 m above the surface and uses a current waveform with a 4000 μs on-time and data db_z/dt measured during the off-time from 90 to 6340 μs (27 channels) as illustrated in Figure A-1b. A chargeable pipe embedded in the half-space earth is shown in Figure A-1a. The conductivity of the half-space, σ_{half} is 10^{-4} S/m, and Pelton's Cole-Cole parameters of the chargeable cylinder are $\sigma_\infty = 6 \times 10^{-2}$ S/m, $\eta = 0.15$, $\tau = 1600$ μs, and $c = 0.5$. Using the EMTDIP code Marchant et al. (2014), we perform two forward modelings to compute observed $F[\sigma(t)]$ and the fundamental responses $F[\sigma_\infty]$. These are subtracted to yield d^{IP}. In Figure 6, the black, blue, and red lines correspondingly show d, $F[\sigma_\infty]$, and d^{IP} responses. The solid and dashed lines distinguish positive and negative data.

References

Boyko, W., N. R. Paterson, and K. Kwan, 2001, AeroTEM: System characteristics and field results: The Leading Edge, **20**, 1130–1138, doi: 10.1190/1.1487244.

Cockett, R., S. Kang, L. J. Heagy, A. Pidlisecky, and D. W. Oldenburg, 2015, SimPEG: An open source framework for simulation and gradient based parameter estimation in geophysical applications: Computers & Geosciences, **85**, 142–154, doi: 10.1016/j.cageo.2015.09.015.

Cole, K. S., and R. H. Cole, 1941, Dispersion and absorption in dielectrics I. Alternating current characteristics: The Journal of Chemical Physics, 9, 341, doi: 10.1063/1.1750906.

Devriese, S. G. R., K. Davis, and D. W. Oldenburg, 2017, Inversion of airborne geophysics over the DO-27/DO-18 kimberlites — Part 1: Potential fields: Interpretation, **5**, this issue, doi: 10.1190/int-2016-0142.1.

Doyle, B. J., K. Kivi, and B. H. S. Smith, 1999, The Tli Kwi Cho (DO27 and DO18) diamondiferous kimberlite complex, Northwest Territories, Canada: Proceedings of the 7th International Kimberlite Conference, 194–204.

Eggleston, T., and K. Brisebois, 2008, Do-27 diamond project, northwest territories, Canada: Ni 43-101 Report, AMEC.

El-Kaliouby, H., and E. Eldiwany, 2004, Transient electromagnetic responses of 3D polarizable body: Geophysics, **69**, 426–430, doi: 10.1190/1.1707062.

Flores, C., and S. A. Peralta-Ortega, 2009, Induced polarization with in-loop transient electromagnetic soundings:

A case study of mineral discrimination at El Arco porphyry copper, Mexico: Journal of Applied Geophysics, **68**, 423–436, doi: 10.1016/j.jappgeo.2009.03.009.

Fournier, D., S. Kang, M. S. Michael, and D. W. Oldenburg, 2017, Inversion of airborne geophysics over the DO-27/DO-18 kimberlites — Part 2: Electromagnetics: Interpretation, **5**, this issue, doi: 10.1190/int-2016-0140.1.

Grimm, R. E., and D. E. Stillman, 2015, Field test of detection and characterization of subsurface ice using broadband spectral induced polarization: Permafrost and Periglacial Processes, **26**, 28–38.

Harder, M., C. M. Hetman, B. H. S. Smith, and J. Pell, 2008, The evolution of geological models for the DO-27 kimberlite, NWT, Canada: Implications for evaluation: Presented at the 9th International Kimberlite Conference.

Jansen, J. C., and B. J. Doyle, 1998, The tli kwi cho kimberlite comples, northwest territories, canada: a geophysical post mortem: Presented at the NWMA Pratical Geophysics Short Course, Northwest Mining Association.

Kang, S., and D. W. Oldenburg, 2016, On recovering distributed IP information from inductive source time domain electromagnetic data: Geophysical Journal International, **207**, 174–196, doi: 10.1093/gji/ggw256.

Kang, S., D. Oldenburg, D. Yang, and D. Marchant, 2014, On recovering induced polarization information from airborne time domain EM data: 84th Annual International Meeting, SEG, Expanded Abstracts, 1785–1789.

Kozhevnikov, N., and E. Antonov, 2012, Fast-decaying inductively induced polarization in frozen ground: A synthesis of results and models: Journal of Applied Geophysics, **82**, 171–183, doi: 10.1016/j.jappgeo.2012.03.008.

Kratzer, T., and J. Macnae, 2012, Induced polarization in airborne EM: Geophysics, **77**, no. 5, E317–E327, doi: 10.1190/geo2011-0492.1.

Macnae, J., 2015, Quantifying airborne induced polarization effects in helicopter time domain electromagnetics: Journal of Applied Geophysics, **135**, 495–502.

Marchant, D., E. Haber, and D. Oldenburg, 2014, Three-dimensional modeling of IP effects in time-domain electromagnetic data: Geophysics, **79**, no. 6, E303–E314, doi: 10.1190/geo2014-0060.1.

Pelton, W., S. Ward, P. Hallof, W. Sill, and P. Nelson, 1978, Mineral discrimination and removal of inductive coupling with multifrequency IP: Geophysics, **43**, 588–609, doi: 10.1190/1.1440839.

Power, M., and D. Hildes, 2007, Geophysical strategies for kimberlite exploration in northern Canada: Proceedings of Exploration 2007: Fifth Decennial International Conference on Mineral Exploration, 1025–1031.

Revil, A., N. Florsch, and C. Camerlynck, 2014, Spectral induced polarization porosimetry: Geophysical Journal International, **198**, 1016–1033, doi: 10.1093/gji/ggu180.

Smith, R. S., 1988, A plausible mechanism for generating negative coincident-loop transient electromagnetic responses: Ph.D. thesis, University of Toronto.

Smith, R. S., and J. Klein, 1996, A special circumstance of airborne induced-polarization measurements: Geophysics, **61**, 66–73, doi: 10.1190/1.1443957.

Smith, R. S., P. Walker, B. Polzer, and G. F. West, 1988, The time-domain electromagnetic response of polarizable bodies: An approximate convolution algorithm: Geophysical Prospecting, **36**, 772–785, doi: 10.1111/j.1365-2478.1988.tb02192.x.

Smith, R. S., and G. F. West, 1989, Field examples of negative coincident-loop transient electromagnetic responses modeled with polarizable half-planes: Geophysics, **54**, 1491–1498, doi: 10.1190/1.1442613.

Weidelt, P., 1982, Response characteristics of coincident loop transient electromagnetic systems: Geophysics, **47**, 1325–1330, doi: 10.1190/1.1441393.

Seogi Kang received an M.S. (2012) in geophysics from Hanyang University, South Korea. He is a Ph.D. candidate in geophysics at the University of British Columbia, Canada. His research interests include extracting induced polarization information from various electromagnetic data. He is one of the main contributors to an open-source geophysical inversion pacakge: SimPEG (http://www.simpeg.xyz/).